Relationship between Warm Airmass Transport into the Upper Polar Atmosphere and Cold Air Outbreaks in Winter

YUEYUE YU

Department of Earth, Ocean and Atmospheric Science, Florida State University, Tallahassee, Florida, and LASG, Institute of Atmospheric Physics, and University of Chinese Academy of Sciences, Beijing, China

MING CAI

Department of Earth, Ocean and Atmospheric Science, Florida State University, Tallahassee, Florida

RONGCAI REN

LASG, Institute of Atmospheric Physics, Chinese Academy of Sciences, Beijing, China

HUUG M. VAN DEN DOOL

NOAA/NCEP/NWS/Climate Prediction Center, College Park, Maryland

ABSTRACT

This study investigates dominant patterns of daily surface air temperature anomalies in winter (November–February) and their relationship with the meridional mass circulation variability using the daily Interim ECMWF Re-Analysis in 1979–2011. Mass circulation indices are constructed to measure the day-to-day variability of mass transport into the polar region by the warm air branch aloft and out of the polar region by the cold air branch in the lower troposphere. It is shown that weaker warm airmass transport into the upper polar atmosphere is accompanied by weaker equatorward advancement of cold air in the lower troposphere. As a result, the cold air is largely imprisoned within the polar region, responsible for anomalous warmth in midlatitudes and anomalous cold in high latitudes. Conversely, stronger warm airmass transport into the upper polar atmosphere is synchronized with stronger equatorward discharge of cold polar air in the lower troposphere, resulting in massive cold air outbreaks in midlatitudes and anomalous warmth in high latitudes. There are two dominant geographical patterns of cold air outbreaks during the cold air discharge period (or 1–10 days after a stronger mass circulation across 60°N). One represents cold air outbreaks in midlatitudes of both North America and Eurasia, and the other is the dominance of cold air outbreaks only over one of the two continents with abnormal warmth over the other continent. The first pattern mainly corresponds to the first and fourth leading empirical orthogonal functions (EOFs) of daily surface air temperature anomalies in winter, whereas the second pattern is related to the second EOF mode.

1. Introduction

Both extreme cold and warm temperature events in winter are potentially severe weather phenomena that have a serious influence on residents, agriculture, and transportation. Cold air outbreaks in the southeastern states of the United States are closely related to Florida citrus freezes (Rogers and Rohli 1991; Downton and Miller 1993), whereas successive cold air outbreaks induced by the Siberian high often lead to severe frost, freezing rain, or heavy snowfalls over eastern China, Korea, and Japan (Boyle and Chen 1987; Chan and Li 2004). Pest populations tend to increase in a warm winter, reducing crop yields (Rosenzweig et al. 2001). Anomalously warm events in winter also adversely affect winter transportation, flooding, and the skiing industry (Shabbar and Bonsal 2003). Associated with the increasing global-mean temperature, there is an increasing trend in the occurrence of anomalously warm

events in winter seasons but little decreasing trend in the occurrence frequencies of extreme cold events over the northeastern United States (Kunkel et al. 1999; Walsh et al. 2001; Portis et al. 2006), Europe (Thompson 1987; Brugge 1991; Walsh et al. 2001), and most of Asia (Gong and Ho 2004). Therefore, revealing the underlying dynamic and physical processes and improving the predictability of both extreme cold and warm events in winter seasons deserve special attention.

The location, intensity, and evolution of extreme temperature events are highly variable on synoptic scales. The main synoptic- and planetary-scale precursors to cold air outbreaks in North America include the variability of polar anticyclones (Wexler 1951; Colucci and Davenport 1987), positive sea level pressure anomalies over the Alaska–Yukon border (Walsh et al. 2001), and coupling of the ridge over the Arctic and the trough over the Great Lakes region (Konrad 1996). For cold air surges in Asia, an abrupt expansion of the Siberian high toward East Asia plays a key role in the initiation of cold air surges (Ding 1990; Zhang et al. 1997; Gong and Ho 2004; Takaya and Nakamura 2005). The expansion and amplification of the Siberian high are modulated by the upper-tropospheric circulation systems including blockings and stationary Rossby wave trains propagating across Eurasia (Takaya and Nakamura 2005; Jeong et al. 2006; Park et al. 2008). There is also ample evidence indicating that extreme cold events are linked to leading teleconnection patterns in the extratropical tropospheric winter. The North Atlantic Oscillation (NAO) tends to be in its negative phase 3–6 days prior to the onset of cold air outbreaks over the United States and Eurasia (Walsh et al. 2001; Cellitti et al. 2006). The Arctic Oscillation (AO), or the tropospheric northern annular mode (NAM), also has a close relation with extreme temperature events in winter over Eurasia and North America on intraseasonal and longer time scales (Thompson and Wallace 1998; Thompson and Wallace 2001; Wettstein and Mearns 2002; Cohen et al. 2010). These teleconnection patterns are all associated with variations in the zonal-mean zonal wind. The latter has been referred to as the index cycle following the pioneering study of Namias (1950) on the linkage of cold air outbreaks in winter to variations of the westerly jet in the extratropical troposphere.

Stratospheric circulation anomalies and tropical forcing have been found to be promising precursors to extreme cold events in midlatitudes. Extreme cold events in eastern North America, northern Europe, and eastern Asia tend to take place more frequently in the period of 1–2 months after a weaker stratospheric polar vortex (Baldwin and Dunkerton 1999; Wallace 2000; Thompson et al. 2002). Kolstad et al. (2010) found that cold temperature anomalies tend to occur over the southeastern United States 1–2 weeks after the peak day of weak vortex events, whereas cold anomalies occur over Eurasia at the inception of weak vortex events. Cai (2003) reported that cold temperature anomalies tend to take place over the regions underneath the intrusion of the stratospheric air into the troposphere (or tropopause foldings). The easterly phase of the quasi-biannual oscillation (QBO) in the equatorial stratosphere is favorable for below-normal winter-mean temperature over most of the two continents (Thompson et al. 2002; Cai 2003). The warm phase of ENSO events favors cold anomalies in the southeastern United States (e.g., Kiladis and Diaz 1989; Thompson et al. 2002; Kenyon and Hegerl 2008), whereas the MJO-associated convection located over the Indian Ocean favors more extreme cold air surge events in East Asia in winter (Jeong et al. 2005).

The pioneering work of Johnson and his collaborators (Johnson 1989) and many subsequent studies (e.g., Cai and Shin 2014, and references therein) have documented the existence of the global meridional mass circulation system that connects the tropics to the poles and the troposphere to the stratosphere via the poleward warm air branch in the upper troposphere (as well as the winter hemisphere's stratosphere) and the equatorward cold branch in the lower troposphere.[1] Cai and Ren (2007) and Ren and Cai (2007, 2008) have postulated that the poleward-propagating, positive, stratospheric temperature anomalies are associated with a stronger warm air branch of the meridional mass circulation and vice versa. The negative phase of stratospheric NAM events is associated with a stronger poleward mass circulation, whereas the positive phase is associated with a weaker circulation. Because the poleward propagation in the upper stratosphere tends to be ahead of that in the lower stratosphere, there exists a downward propagation of stratospheric anomalies of both signs associated with stratospheric NAM events. The variability of the compensating cold air branch is synchronized with that of the warm air branch, responsible for the equatorward propagation of negative tropospheric temperature anomalies following the arrival of the poleward-propagating positive temperature anomalies in the polar stratosphere. Such synchronization between the two branches is expected from meridional mass circulation theory, namely, that vertically westward-tilted baroclinic waves are responsible for both a net poleward mass transport aloft and a simultaneous net equatorward mass

---

[1] We refer to the poleward branch in the upper troposphere as the warm air branch and the equatorward branch in the lower troposphere as the cold air branch in terms of the potential temperature that always increases with height in a stably stratified atmosphere.

transport below (e.g., Johnson 1989). The extra air mass brought to the polar region by a stronger poleward mass circulation contributes to a rising of the surface pressure over the Arctic before the cold air in the lower polar troposphere is carried out by a stronger equatorward cold air branch. This explains why the AO or tropospheric NAM tends to be nearly in phase with the lower-stratospheric NAM. Recently, Iwasaki and Mochizuki (2012) and Iwasaki et al. (2014) identified two climatological-mean routes or main streams of cold air from the polar region to lower latitudes within the cold air branch of the meridional mass circulation, namely, the ''East Asian stream'' and the ''North American stream.'' The East Asian stream intensifies over the northern part of Eurasia while flowing eastward. It then turns southeastward toward East Asia via Siberia and dissipates over the western North Pacific Ocean. The North American stream intensifies over the Arctic Ocean and moves toward the east coast of North America via the Hudson Bay and dissipates over the western North Atlantic Ocean.

The primary objective of this study is to develop meridional mass circulation indices on a daily basis to directly and physically link atmospheric circulation anomalies to individual cold air outbreak events in midlatitudes in winter with statistically robust lead and lag information. Toward this goal, we will construct indices that measure the intensity of the meridional mass circulation crossing a latitude circle between midlatitudes and the polar region using the data produced by the Interim European Centre for Medium-Range Weather Forecasts Re-Analysis (ERA-Interim). To the authors' knowledge, mass-circulation-based indices used as precursors for winter cold air outbreaks have not been systematically investigated before. The two phrases ''stronger mass circulations out of the polar region'' and ''cold air outbreaks'' may be regarded as synonymous to one another since the former is the leading physical cause of cold temperature anomalies in midlatitudes besides anomalous diabatic cooling owing to radiative processes and surface sensible heat fluxes. We will examine whether the day-to-day variability of mass transport into and out of the polar region can serve as a robust precursor to massive cold air outbreak events in midlatitudes and identify dominant spatial patterns of surface air temperature anomalies closely related to large amplitude events of the meridional mass circulation variability in winter seasons.

This paper is organized as follows: Section 2 describes the dataset used in this study and defines indices for the mass circulation as well as for large-amplitude surface air temperature anomalies in high and midlatitudes. In section 3, we investigate the temporal lead–lag relation and probability distribution of temperature area indices in the mid- and high latitudes with mass circulation indices. Section 4 examines the mean geographical patterns of surface air temperature anomalies associated with different intensities of the meridional mass circulation. In section 5, we link the dominant empirical orthogonal function (EOF) modes of daily surface air temperature anomalies in winter seasons to the day-to-day variability of mass circulation. The concluding remarks are provided in section 6.

2. Data and methodology

The data used in this study include daily surface air temperature, surface pressure, and three-dimensional air temperature and wind fields derived from the daily ERA-Interim data for the period from 1 November 1979 to 28 February 2011 (Dee et al. 2011). The data fields are on 1.5° latitude × 1.5° longitude grids with 37 pressure levels spanning from 1000 to 1 hPa. Each of the 32 winters lasts 120 days from 1 November of the current year to 28 February of the next year.

a. Indices of meridional mass transport into and out of the polar region

The eddy-driven meridional circulation in the extratropics can be obtained through the transformed Eulerian-mean (TEM) formulation, as first proposed by Andrews and McIntyre (1976). Johnson and his collaborators (e.g., Gallimore and Johnson 1981; Townsend and Johnson 1985; Johnson 1989) first diagnosed the time- and zonal-mean mass circulation in isentropic coordinates. By explicitly taking the zonal variation of atmospheric mass associated with waves into consideration, they showed a single thermally direct circulation cell in each hemisphere that links the heat source in the tropics to the heat sink in high latitudes. As explicitly proved in Pauluis et al. (2011), the extratropical portion of the time-mean isentropic meridional mass circulation calculated from instantaneous total fields is almost indistinguishable from the time-mean eddy-driven circulation inferred from the TEM formulation in the pressure coordinate.

In this study, we follow the isentropic mass circulation framework to diagnose the meridional mass circulation from instantaneous total fields on a daily basis without the decomposition of the time-mean and transient flows and without the separation of zonal-mean and wavy flows. Specifically, following Pauluis et al. (2008, 2010), we first interpolate daily air temperature and wind fields onto 200 equally spaced sigma (σ) levels from 1 to 0. The air mass m_σ between two adjacent sigma surfaces per unit area is

$$m_\sigma = \frac{\Delta\sigma}{g} P_s, \qquad (1)$$

where P_s is the surface pressure (Pa), g is the gravitational acceleration, and $\Delta\sigma = 1/200$. We then derive the meridional mass flux between adjacent isentropic surfaces (Θ_n and Θ_{n+1}) in each grid at latitude ϕ and longitude λ, on day t as

$$F_m(\lambda, \phi, \Theta_n, t) = \int_0^1 m_\sigma v Y(\theta, \Theta_n, \Theta_{n+1}) \, d\sigma, \qquad (2)$$

where $Y(\theta, \Theta_n, \Theta_{n+1}) = 1$ for $(\Theta_n \leq \theta < \Theta_{n+1})$, and otherwise $Y(\theta, \Theta_n, \Theta_{n+1}) = 0$. In (2), $v(\lambda, \phi, \sigma, t)$ is the meridional wind and $\theta(\lambda, \phi, \sigma, t)$ is the potential temperature field evaluated from air temperature and pressure fields; Θ_n is equal to $\theta_{\min}(\lambda, \phi, t)$ or one of the 15 preselected potential temperature surfaces that is above $\theta_{\min}(\lambda, \phi, t)$, whereas Θ_{n+1} is one of the 15 preselected potential temperature surfaces that is just above Θ_n or $\theta_{\max}(\theta_{\max} > 1200\,\text{K})$. The 15 preselected isentropic surfaces are 260, 270, 280, 290, 300, 315, 330, 350, 370, 400, 450, 550, 650, 850, and 1200 K. The layer between $\theta_{\min}(\lambda, \phi, t)$ and 260 K is labeled as the 250-K layer. We note that $\theta_{\min}(\lambda, \phi, t)$ is defined as the minimum value of $\theta(\lambda, \phi, \sigma, t)$, equal to the surface potential temperature unless a superadiabatic layer exists near the surface.

We next obtain the zonally integrated meridional mass flux field $\overline{F_m(\lambda, \phi, \Theta_n, t)}^\lambda$ by integrating the meridional mass flux fields obtained from (2) along each latitude belt. The field of $\overline{F_m(\lambda, \phi, \Theta_n, t)}^\lambda$ represents the total mass transport across each latitude ϕ in each

isentropic layer (Θ_n and Θ_{n+1}) at time t. For an easy reference, we just refer to the latitude band inside 60°N as the polar region in this paper. The case of $\overline{F_m(\lambda, \phi = 60°N, \Theta_n, t)}^\lambda > 0$ corresponds to a net mass transport into the polar region in the layer between Θ_n and Θ_{n+1}, and the case of $\overline{F_m(\lambda, \phi = 60°N, \Theta_n, t)}^\lambda < 0$ corresponds to a net mass transport out of the polar region in the layer between Θ_n and Θ_{n+1}.

In general, in the Northern Hemisphere, negative values of $\overline{F_m(\lambda, \phi, \Theta_n, t)}^\lambda$ are found in the lower troposphere within the equatorward cold air branch of the meridional mass circulation, whereas positive values are in upper layers, belonging to the poleward warm air branch. According to the climatological-mean structure of meridional mass circulation in the Northern Hemispheric winter (Cai and Shin 2014), the isentropic layer separating the warm air branch and the cold air branch near 60°N is about 280 K, which is also the threshold potential temperature of climatological-mean cold air used by Iwasaki et al. (2014). In this study, we search for $\Theta_{n*}(t)$ at 60°N at time t such that the vertical sum of $\overline{F_m(\lambda, \phi = 60°N, \Theta_n, t)}^\lambda$ for all $n < n*$ or $\Theta_n < \Theta_{n*}$ reaches its maximum negative value. It follows that $\Theta_{n*}(t)$ corresponds to the boundary separating the poleward warm branch aloft from the equatorward cold branch below. It is found that $\Theta_{n*}(t)$ most often lies between 270 and 290 K, consistent with previous studies. Using $\Theta_{n*}(t)$, we define the following two mass circulation indices measuring the total airmass transport across 60°N into the polar region (denoted as WB60N and CB60N, respectively):

$$\text{WB60N}(t) = \frac{\overline{\sum_{\Theta_n=\Theta_{n*}}^{\Theta_{\max}} \overline{F_m(\lambda, \phi = 60°N, \Theta_n, t)}^\lambda}^\tau - \left\{ \overline{\sum_{\Theta_n=\Theta_{n*}}^{\Theta_{\max}} \overline{F_m(\lambda, \phi = 60°N, \Theta_n, t)}^\lambda}^\tau \right\}}{\text{SD}^W}$$

$$\text{CB60N}(t) = \frac{\overline{\sum_{\Theta_n=\Theta_{\min}}^{\Theta_{n*-1}} \overline{-F_m(\lambda, \phi = 60°N, \Theta_n, t)}^\lambda}^\tau - \left\{ \overline{\sum_{\Theta_n=\Theta_{\min}}^{\Theta_{n*-1}} \overline{-F_m(\lambda, \phi = 60°N, \Theta_n, t)}^\lambda}^\tau \right\}}{\text{SD}^C}, \qquad (3)$$

where the overbar with the superscript τ denotes a 7-day running mean at time t from $(t-3)$ to $(t+3)$ days. The term

$$\left\{ \overline{\sum_{\Theta_n=\Theta_{n*}}^{\Theta_{\max}} \overline{F_m(\lambda, \phi = 60°N, \Theta_n, t)}^\lambda}^\tau \right\}$$

denotes the time average of

$$\overline{\sum_{\Theta_n=\Theta_{n*}}^{\Theta_{\max}} \overline{F_m(\lambda, \phi = 60°N, \Theta_n, t)}^\lambda}^\tau$$

over the 32 winters from 1979 to 2011 for each calendar day between 1 November and 28 February, forming

a 120-day time series of winter-season daily climatology of the total mass transport crossing 60°N into the polar region in the poleward warm air branch. Similarly, the term

$$\left\{ \overline{\sum_{\Theta_n = \Theta_{\min}}^{\Theta_{n*-1}} \overline{-F_m(\lambda, \phi = 60°N, \Theta_n, t)}^{\lambda}}^{\tau} \right\}$$

is the 120-day time series of winter-season daily climatology of total mass transport crossing 60°N out of the polar region in the equatorward cold air branch. In (3), $SD^W = 16.43 \times 10^9 \, kg\,s^{-1}$ and $SD^C = 16.92 \times 10^9 \, kg\,s^{-1}$, corresponding to, respectively, the standard deviations (SDs) of the two time series represented by the numerators in these 32 winters. Therefore, the WB60N (CB60N) index measures the normalized anomalous mass transport into (out of) the polar region by the warm (cold) air branch at time t averaged over from $(t - 3)$ to $(t + 3)$.

b. Warmth and cold area indices

The climatological-mean surface air temperature (SAT) fields were obtained by averaging the data across the 32 years (1979–2011) for each calendar day from 1 November to 28 February. Daily surface air temperature anomalies (SATA hereafter) were obtained by removing the daily climatology from the total field and then applying a 7-day running-mean filtering. The local standard deviation (LSD) of SATA was obtained from the 32-yr mean of the root-mean-square of SATA at each grid point for each calendar day from 1 November to 28 February.

Following Cai (2003), we define four temperature (warmth and cold) area indices to measure the spatial extent or area occupied by warm and cold anomalies exceeding 0.5 LSD in mid- and high latitudes. Specifically, the warmth and cold area indices for high latitudes, denoted as $W_H(t)$ and $C_H(t)$, respectively, are defined as

$$W_H(t) = \frac{\int_A H(\text{SATA} - 0.5\text{LSD})\,dA}{\int_A dA};$$

$$C_H(t) = \frac{\int_A H(0.5\text{LSD} - \text{SATA})\,dA}{\int_A dA}, \qquad (4)$$

where $\int_A dA$ denotes an area integral over the area A covering the domain 60°–90°N and $H(x)$ is the Heaviside function such that $H(x) = 1$ for $x > 0$; otherwise $H(x) = 0$. Similarly, the warm and cold area indices for midlatitudes, denoted as $W_H(t)$ and $C_H(t)$, can be defined

using (4), except that A is the domain 25°–60°N. We have tested other choices of the threshold, such as 0.0 LSD and 1.0 LSD and found that the results are not sensitive to the choice of the threshold. We also have tested 55°–65°N for the southernmost boundary of high latitudes and 20°–30°N for that of midlatitudes and found that main characteristics of the results remain unchanged.

3. Relations of warmth and cold area indices with mass circulation indices

The extratropical atmospheric circulation is largely in geostrophic balance. As a result, the extratropical meridional circulation has to be very weak in the absence of waves (by definition, the zonal-mean meridional geostrophic flow is zero). The mechanism for the simultaneous poleward mass flux aloft and equatorward mass flux below in the extratropics has been uniquely attributed to the wave dynamics of baroclinic instability (Johnson 1989). Being in hydrostatic balance and (quasi) geostrophic balance, westward-tilted baroclinic waves always transport more air mass poleward in front of the troughs than equatorward behind the troughs in upper levels, but transport more air mass equatorward behind the troughs than poleward in front of the troughs in lower levels. The net effect of westward-tilted baroclinic waves is simultaneous occurrence of the poleward mass transport in upper levels and the equatorward mass transport in lower levels. It follows that stronger activity of westward-tilted waves in the extratropics would result in stronger meridional mass circulation, causing a simultaneous increase in both the poleward mass transport into the polar region aloft and the equatorward mass transport out of the polar region in the lower troposphere. The nearly perfect synchronization of the time series of the daily CB60N index with the WB60N index, in terms of both timing and amplitude (not shown), indicates that the anomalous mass brought out of the polar region by the cold air branch is nearly in balance with the anomalous mass brought into the polar upper atmosphere by the warm air branch of the meridional mass circulation at daily time scales. The difference between them, which is at least one order of magnitude smaller than either WB60N or CB60N, nearly corresponds to the daily local tendency of the surface pressure over the polar region.[2] Hence, we use the WB60N index to represent daily variations of the

---

[2] One needs also to consider the hydrological cycle, that is, moisture transport, evaporation, and precipitation, to fully account for the surface pressure tendency as pointed out by Trenberth (1991) and van den Dool and Saha (1993).
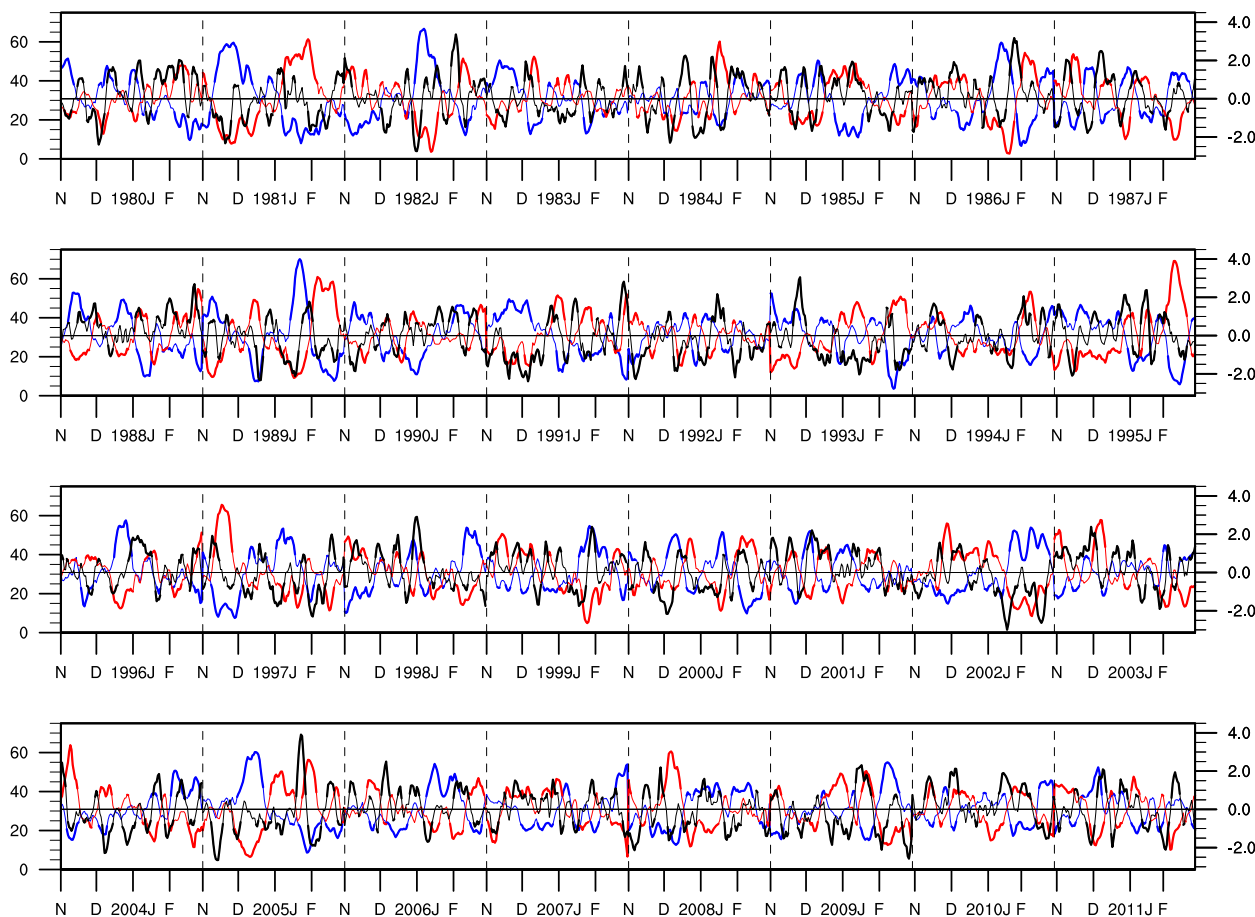
FIG. 1. Time series of WB60N (black), C_H (blue), and W_H (red) indices in the 32 winters from November 1979 to February 2011. The ordinate on the right is for the WB60N index with one unit representing the poleward mass flux anomaly of $16.43 \times 10^9\,\mathrm{kg\,s^{-1}}$ crossing 60°N. The ordinate on the left is for C_H and W_H indices (%). The horizontal line represents the constant of 30.85% for C_H and W_H indices, which corresponds to the fractional area of a given domain occupied by SATA exceeding 0.5 LSD (either positively or negatively under a normal Gaussian distribution). The thick portions of C_H and W_H correspond to the periods when their values (relative to 30.85%) exceed 0.5 standard deviations of the time series of C_H and W_H (one standard deviation is 11.31% for C_H and 10.79% for W_H). The dashed vertical bars are for dividing winters between two adjacent years.

meridional mass circulation crossing 60°N with positive values corresponding to a stronger meridional mass circulation and negative for a weaker meridional mass circulation.

To illustrate the robust association of temperature area indices with the WB60N index in a case-by-case fashion, we show the time series of W_H (red) and C_H (blue) in Fig. 1 and W_M (red) and C_M (blue) in Fig. 2, superimposed by the time series of WB60N (black). It is seen that in high latitudes, W_H tends to be in phase with WB60N, while C_H tends to be out of phase with WB60N. In midlatitudes, C_M tends to be in phase with WB60N, whereas W_M largely tends to be out of phase with WB60N. It is noteworthy that the variability of the temperature area indices for high latitudes has a wider range (from 0% to 80%) than those for midlatitudes (from 10% to 60%). This suggests that warm events tend

to take place nearly simultaneously over most of the polar region and so do cold events. In midlatitudes, however, temperature anomalies of one polarity in certain areas are always accompanied by temperature anomalies of the opposite polarity elsewhere in the same latitude band, manifesting the role of baroclinic waves in carrying cold air mass equatorward behind the troughs and warm air poleward in front of the troughs.

A close inspection of Figs. 1 and 2 reveals that there are noticeable temporal lags of these four temperature area indices with respect to the WB60N index. To characterize this, we plot in Fig. 3 the correlations of WB60N with each temperature area index in the 32 winters at various time lags (-15 to 15 days). It is seen that large positive correlations between WB60N and W_H or between WB60N and C_M tend to occur when the WB60N index leads by 1–10 days. The same is found for
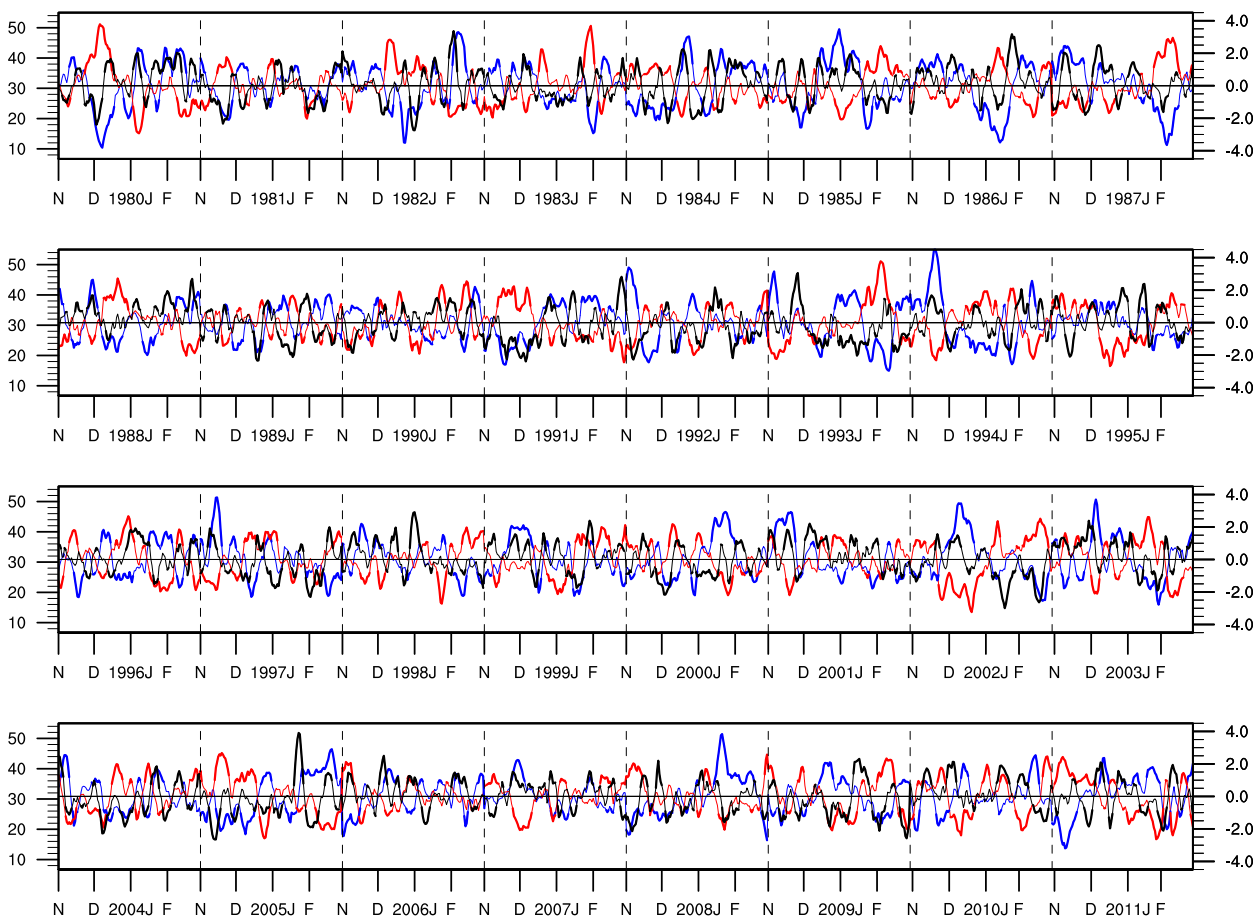
FIG. 2. As in Fig. 1, but for C_M (blue) and W_M (red) indices (one standard deviation is 6.65% for C_M and 6.34% for W_M).

large negative correlations of WB60N with C_H and W_M. We have also confirmed that temporal tendencies of W_H and C_M (C_H and W_M) are highly positively (negatively) correlated with WB60N at lag 0 (not shown). Therefore, the WB60N index does provide temporal lead information (i.e., acts as a precursor) for both massive cold air outbreaks and abnormal warmth in midlatitudes in winter seasons. We note that the correlation of WB60N with W_M is not as strong as with the other three indices. This is probably due not only to a weaker mass transport across the polar circle, but also to a stronger mass transport across the southern boundary of the midlatitude region since both could lead to anomalous warmth in midlatitudes. The lagged correlations shown in Fig. 3 indicate that cold air masses are largely imprisoned within the Arctic in the period of 1–10 days after a weaker meridional circulation crossing 60°N, responsible for general warmth in the midlatitudes and below-normal temperature in high latitudes. Conversely, massive cold air outbreaks in midlatitudes and anomalous warmth in high latitudes tend to take place in the period of 1–10 days after a stronger meridional

circulation crossing 60°N. Based on this and following Namias (1950), we refer to the period of 1–10 days after WB60N above a positive threshold value as the "cold air discharge period," whereas the period of 1–10 days after WB60N below a negative threshold value is referred as the "cold air charge period."

We have constructed a series of probability distribution functions (PDFs) of temperature area indices as a function of the intensity of WB60N in the cold air charge or discharge period. Specifically, we first divided the WB60N index into 10 bins and counted the total number of days for values of WB60N in each of these 10 bins in the 32 winters, which is denoted as $M(k)$, $k = 1, 2, \ldots, 10$ with $k = 1$ corresponding to the case of the weakest and $k = 10$ corresponding to the case of the strongest meridional mass circulation crossing 60°N. Table 1 lists the intervals of the 10 bins, the values of $M(k)$ for all bins, and the ratio of $M(k)$ to the total number of days in these 32 winters as a function of k. Similarly, we divided each temperature area index, after normalizing it with its 32-winter standard deviation, into 10 bins. Taking the C_H index as an example, the histogram of the C_H index can be constructed using
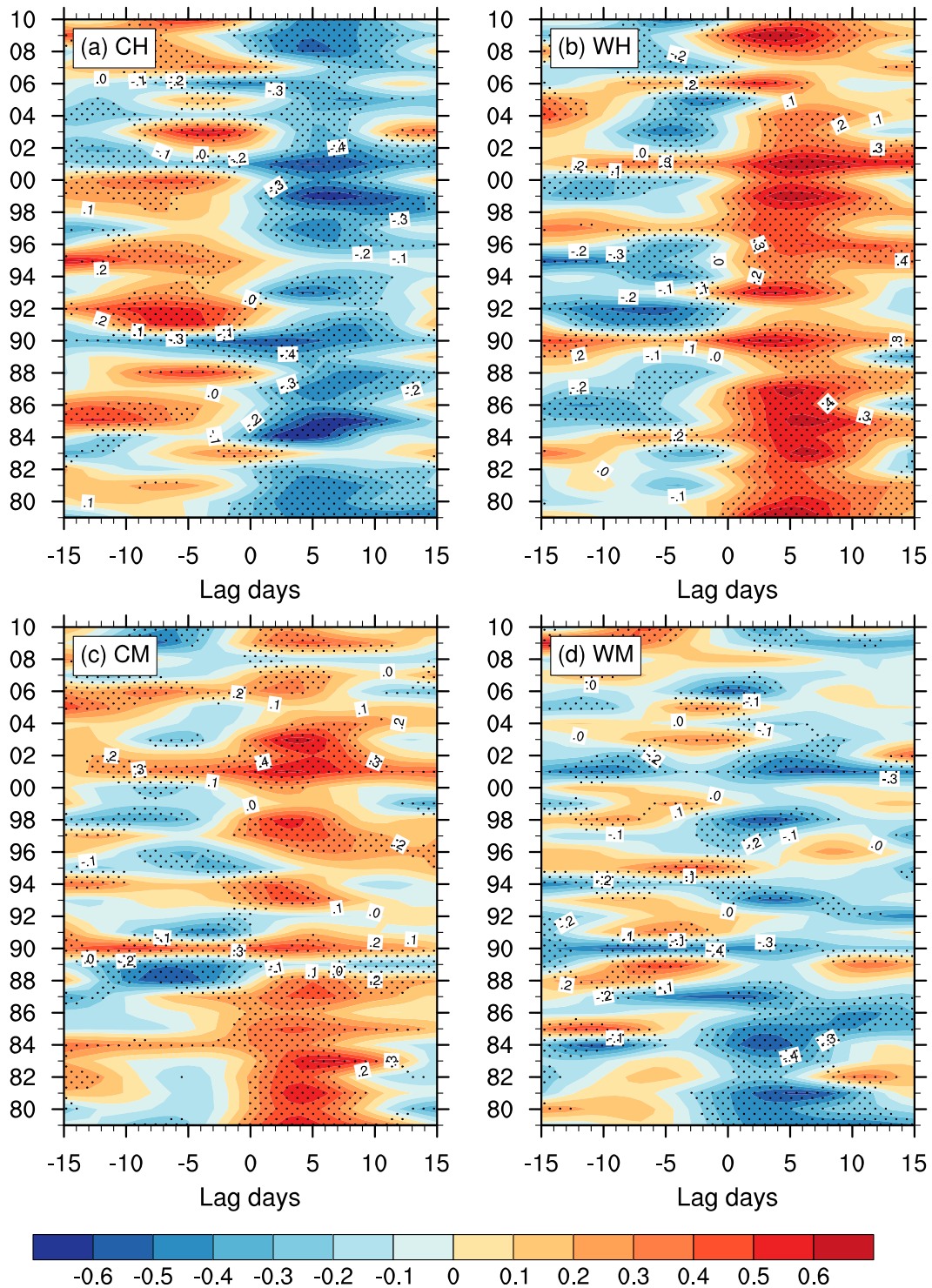
FIG. 3. Lag correlations (−15 to 15 days) of (a) C_H, (b) W_H, (c) C_M, and (d) W_M indices with the WB60N index in each of the 32 winters (ordinate shows the last two digits of the year). Dotted areas indicate correlation exceeding the 95% confidence interval.

TABLE 1. Number of days (M) for the WB60N index in each of the 10 bins and their ratios (P) to 3840 and the total number of days in the 32 winters from November 1979 to February 2011. Note that the WB60N index is the departure of the total poleward mass transport in the warm air branch across 60°N from the climatological means [ranging between 75 and 85×10^9 kg s^{-1} in the months of November–February (NDJF)] normalized by its standard deviation (16.43×10^9 kg s^{-1}).

Bin	WB60N	M (days)	$P = M/3840$
1	$(-\infty, -2]$	86	2.2%
2	$(-2, -1.5]$	159	4.1%
3	$(-1.5, -1]$	378	9.8%
4	$(-1, -0.5]$	568	14.8%
5	$(-0.5, 0]$	719	18.7%
6	$(0, 0.5]$	716	18.6%
7	$(0.5, 1]$	571	14.9%
8	$(1, 1.5]$	400	10.4%
9	$(1.5, 2]$	175	4.6%
10	$(2, +\infty)$	68	1.8%

$$P_{C_H}(j;k) = \frac{N(j;k)}{10M(k)}, \tag{5}$$

where $N(j; k)$ is the total number of days with the normalized C_H index falling into its bin j in the period of 1–10 days after the WB60N index reaches values in its bin k. By definition, the sum of $P_{C_H}(j;k)$ over j from $j = 1$ to $j = 10$ is equal to one for each k. The same procedure has been applied to the other three temperature area indices.

Shown in Fig. 4 are $P_{C_H}(j;k)$, $P_{W_H}(j;k)$, $P_{C_M}(j;k)$, and $P_{W_M}(j;k)$, constructed according to (5), namely, the PDFs of the C_H, W_H, C_M, and W_M indices, respectively. It is seen that, when the meridional mass transport crossing 60°N is normal [i.e., WB60N in $(-0.5, 0.5)$ or $k = 5$ and 6], the PDFs of all the temperature area indices are quasi-normal with the maximum probability centered around their climatological values (30.85%). Therefore, SATA in both high and midlatitudes are in their climatological normal distributions during the period of 1–10 days after a normal meridional mass circulation crossing 60°N. As the intensity of the meridional circulation crossing 60°N is enhanced, there is a pronounced shift of the medians of the quasi-normal PDFs of W_H and C_M toward larger values and those of C_H and W_M toward smaller values. This implies that during the cold air discharge period, the area in midlatitudes occupied by large-amplitude cold SATA (exceeding 0.5 LSD) is far greater than that occupied by large-amplitude warm SATA. Meanwhile, more areas in high latitudes experience large-amplitude warm SATA during the cold air discharge period. Conversely, as the meridional circulation crossing 60°N weakens, there is a pronounced systematic shift of the medians of the

quasi-normal PDFs toward smaller values for W_H and C_M but toward larger values for C_H and W_M. Therefore, in the cold air charge period, there are many more areas in midlatitude exhibiting large-amplitude (exceeding 0.5 LSD) warm temperature anomalies than areas of large-amplitude cold temperature anomalies, while more areas in high latitudes are occupied by large-amplitude cold temperature anomalies.

4. Mean geographical patterns of SATA associated with the WB60N index

To gain insight into the geographical distribution of SATA associated with the meridional mass circulation crossing 60°N, as revealed by these temperature area indices discussed in the previous section, we plot the maps of the probability of SATA exceeding ±0.5 LSD during the cold air charge period (Figs. 5a,b) and the cold air discharge period (Figs. 5c,d). Recall that a deviation of the probability of SATA exceeding ±0.5 LSD from 30.85% by several percentage points implies a noteworthy shift in the PDF from the climatological distribution. In the cold air charge period, most of the polar region experiences abnormal cold as manifested by 38% or higher for the probability of SATA < -0.5 LSD but as low as 22% for the probability of SATA > 0.5 LSD. Meanwhile, most regions in midlatitudes tend to experience general warmth in the cold air charge period by having a probability of 34% or higher for SATA > 0.5 LSD but only 28% or lower for SATA < -0.5 LSD. Nearly opposite spatial patterns of the probability of SATA exceeding ±0.5 LSD are found during the cold air discharge period following a strong meridional mass circulation crossing 60°N (i.e., WB60N > 0.5). It is noteworthy that in high latitudes, cold temperature anomalies after a weaker meridional mass circulation are relatively uniform but the warmth after a stronger meridional mass circulation is more pronounced over the Nordic seas and the Bering Sea. In midlatitudes, the maximum centers of high probability of large-amplitude temperature anomalies are observed over the two continents. The spatial patterns of the high probability of warm temperature anomalies in high latitudes and cold temperature anomalies in midlatitudes in the cold air discharge period seem to suggest that the main routes near the surface for warm air to flow into the Arctic are via two oceans and those for cold air out of the Arctic to midlatitudes are via land, in good agreement with the climatological-mean routes of cold air in winter reported in Iwasaki and Mochizuki (2012) and Iwasaki et al. (2014). In midlatitudes, the reversal of temperature anomalies between the cold air charge and discharge periods is more pronounced over Eurasia, particularly in
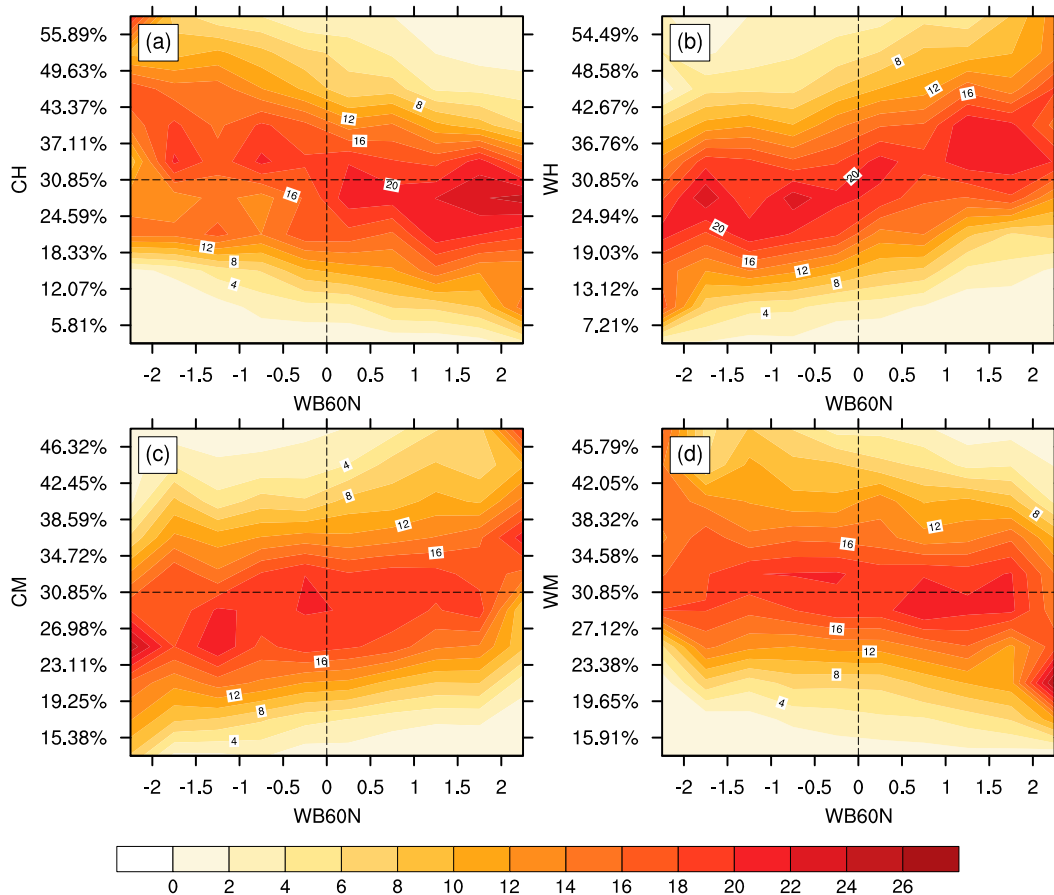
FIG. 4. The conditional probability distribution function (shading, %) of (a) C_H, (b) W_H, (c) C_M, and (d) W_M indices (ordinate) as a function of the intensity of the WB60N index (abscissa). The conditional probability distribution function is constructed for all cases in the period of 1–10 days after the WB60N index reaching a given value (see Table 1 for the total number of cases in the 32 winters for each threshold value of the WB60N index).

eastern Europe, central Asia, and eastern China, than over North America. The region from western Siberia to southeastern China coincides with the westward pathway of cold air surges over East Asia (Wu and Chan 1995; Ryoo et al. 2005; Hayasaki et al. 2006; Iwasaki and Mochizuki 2012; Iwasaki et al. 2014).

The reversal of the geographical pattern of the high probability of positive and negative temperature anomalies between cold air change and discharge periods can also be identified from the composite-mean patterns of SATA. It is seen from Figs. 6a and 6d that SAT is very close to normal (or SATA ∼ 0) everywhere when the meridional circulation crossing 60°N is normal. In the cold air charge period associated with a weaker meridional circulation crossing 60°N (i.e., WB60N < −0.5), negative SATA dominates the polar region surrounded by positive SATA in midlatitudes (Fig. 6b). Positive SATA in midlatitudes is more pronounced over land, especially over Eurasia. Such a spatial pattern of

SATA becomes more pronounced when the meridional circulation crossing 60°N is extremely weak (i.e., WB60N < −1.0, Fig. 6c). A nearly opposite pattern of SATA is found in the cold air discharge period after a stronger meridional circulation crossing 60°N (i.e., WB60N > 0.5 in Fig. 6e and WB60N > 1.0 in Fig. 6f). This demonstrates that in the cold air discharge period, the polar region, on average, experiences anomalous warm with a maximum warm SATA as large as 2 K over the Nordic seas and the Bering Sea, whereas the majority of midlatitudes suffers from cold temperature with minimum cold SATA of −2 K over the central Asia and west Siberia and about −1 K over the U.S. Midwest.

The good agreement in the spatial pattern between the probability (Fig. 5) and composite-mean (Fig. 6) maps indicates that the mean spatial pattern shown in Fig. 6 is representative of the average spatial pattern of SATA in response to day-to-day intensity variations of the meridional mass circulation crossing 60°N. The
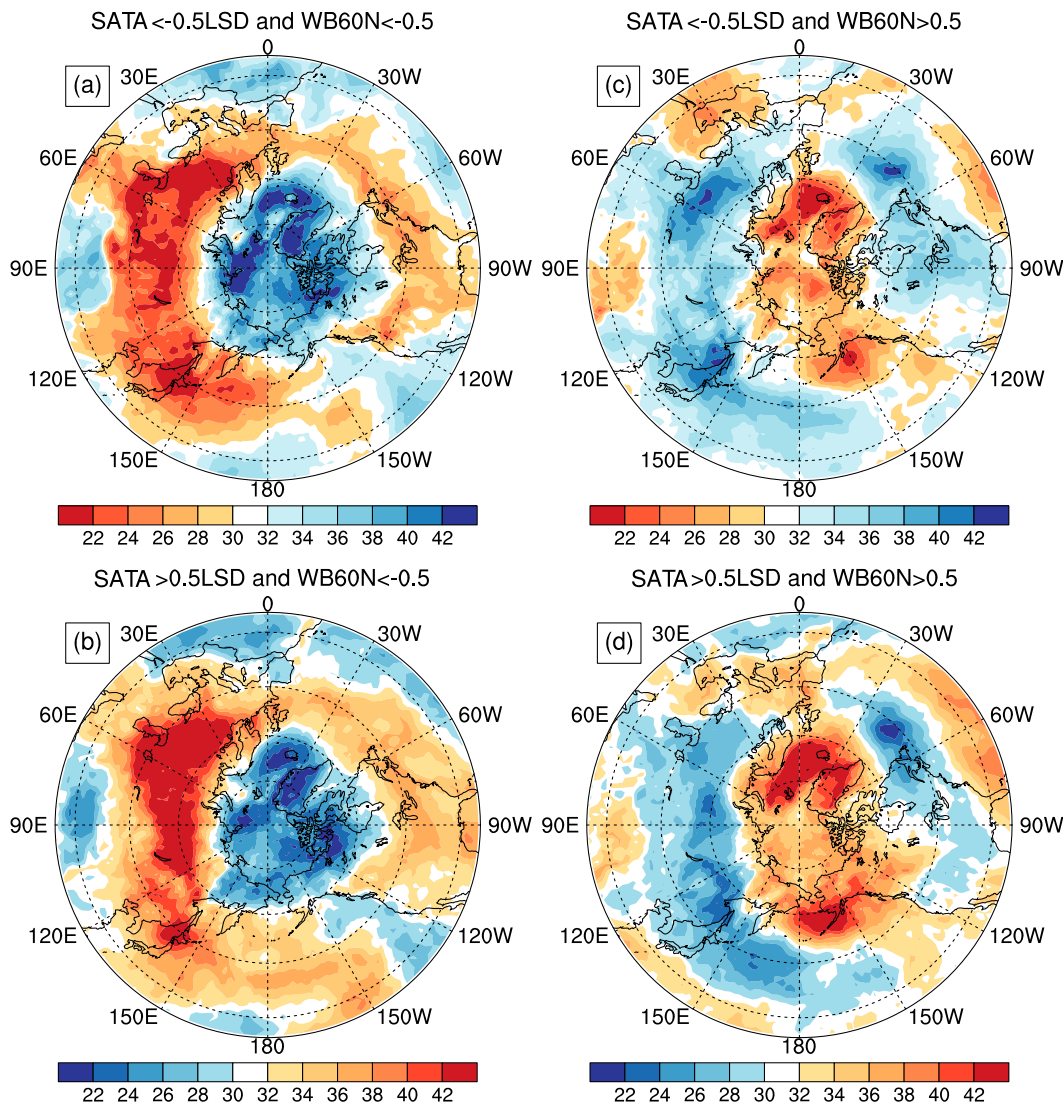
FIG. 5. Geographical pattern of the probability (%, shadings) of (a) SATA < −0.5 LSD and WB60N < −0.5, (b) SATA > 0.5 LSD and WB60N < −0.5, (c) SATA < −0.5 LSD and WB60N > 0.5, and (d) SATA > 0.5 LSD and WB60N > 0.5. The contour value of the white shading is about 30.85%, corresponding to the probability of SATA < −0.5 LSD or SATA > 0.5 LSD for a normal distribution. The probability is constructed for all cases in the period of 1–10 days after the WB60N index reaches the corresponding threshold value (see Table 1 for the total number of cases in the 32 winters for each threshold value of the WB60N index).

case-to-case variations of SATA for the same intensity of WB60N can be quantified by the root-mean-square of departures of SATA from the composite-mean maps. As shown in Fig. 7, the magnitude of the case-to-case variations is several times larger than that of the composite means in most regions. Such large case-to-case differences could reflect either case-to-case amplitude variation of SATA about the mean spatial pattern or the existence of other dominant spatial pattern(s) associated with mass circulation that cannot be captured by a single composite-mean spatial pattern, which is the main subject of the next section.

5. Dominant EOF modes of SATA associated with the WB60N index

An EOF analysis of daily SATA is performed on the domain 25°–90°N for 32 winters from 1979 to 2011. Displayed in Fig. 8 are spatial patterns of the first six EOF modes, which account for up to 50.3% of the total variance of daily SATA over this domain in the 32 winters. The association of the dominant EOF modes of SATA with the meridional mass circulation index can be established by calculating the composite means of the time series of these EOF modes in the period of 1–10
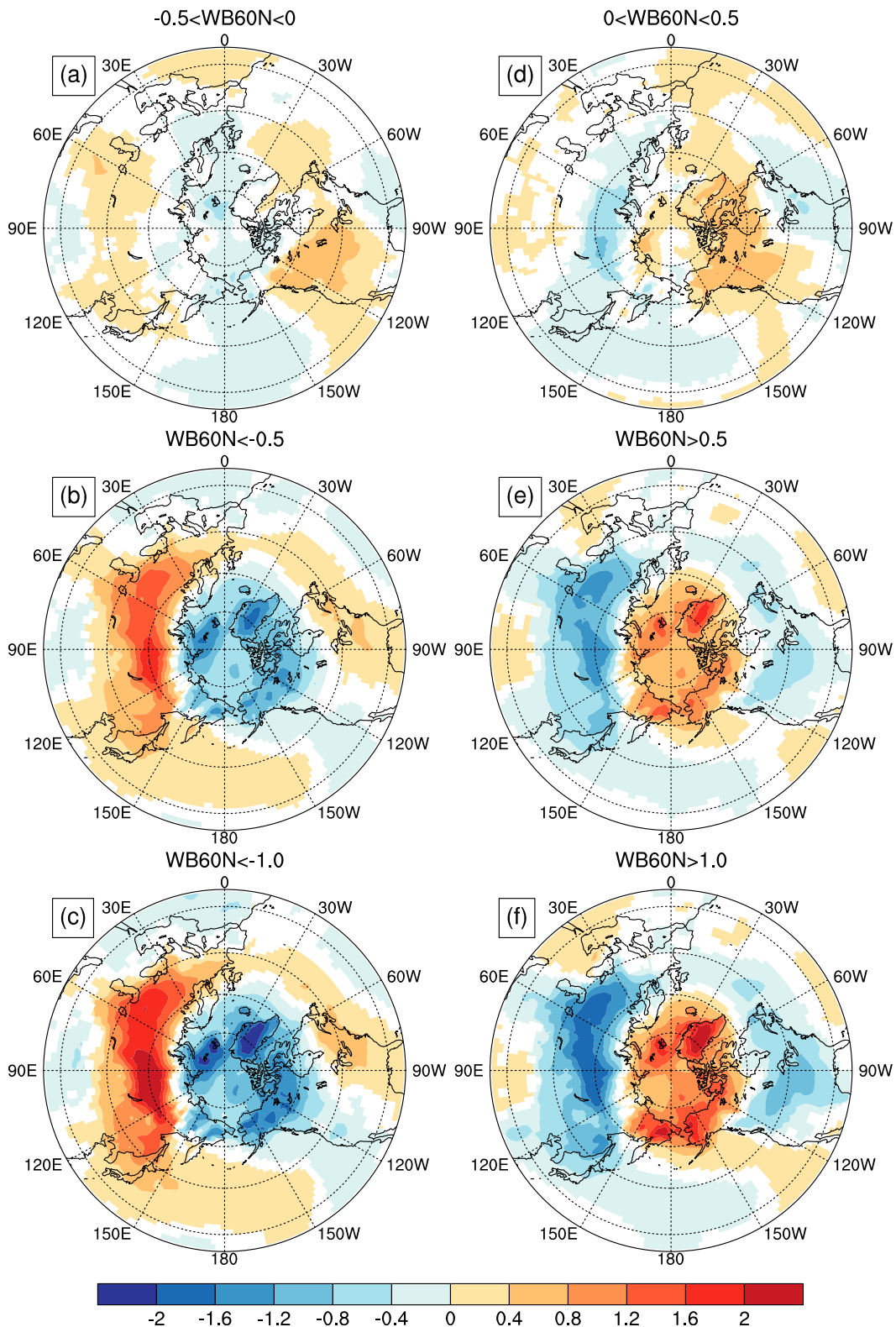
FIG. 6. Maps of composite-mean SATA (K) for cases of (a) $-0.5 < \text{WB60N} < 0$, (b) $\text{WB60N} < -0.5$, (c) $\text{WB60N} < -1.0$, (d) $0 < \text{WB60N} < 0.5$, (e) $\text{WB60N} > 0.5$, and (f) $\text{WB60N} > 1.0$. The results that do not exceed the 95% confidence intervals are not plotted and are represented by the white shading. The composite mean is constructed for all cases in the period of 1–10 days after the WB60N index, reaching the corresponding threshold value (see Table 1 for the total number of cases in the 32 winters for each threshold value of the WB60N index).
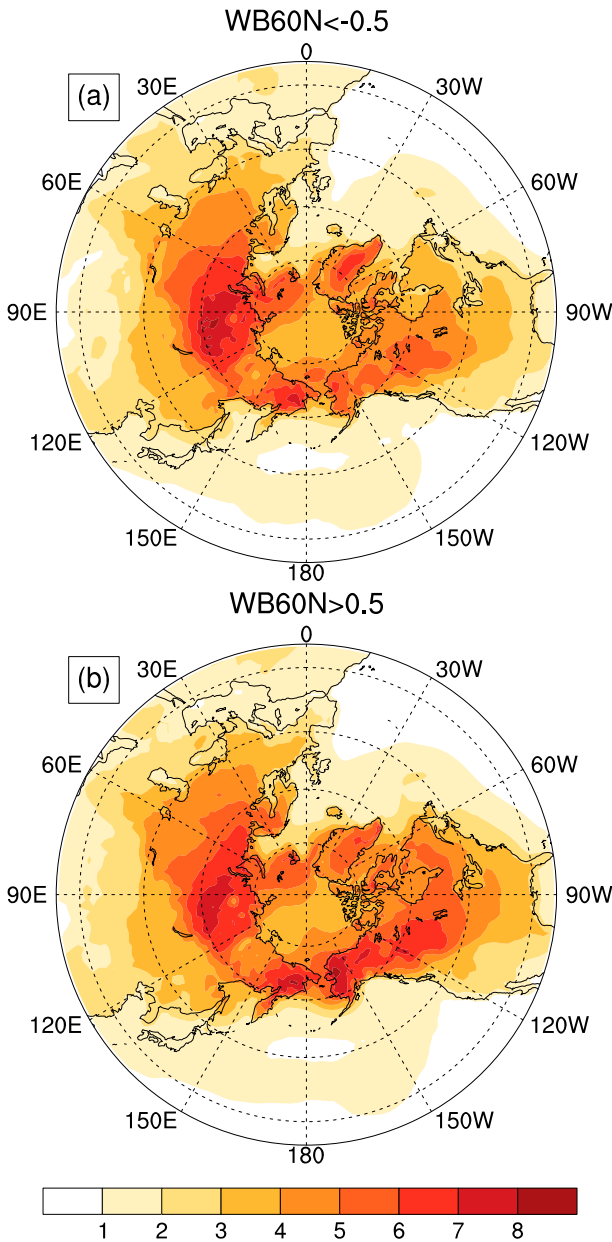
FIG. 7. Standard deviations (K) from the composite-mean SATA for all cases in the period of 1–10 days after (a) WB60N < −0.5 and (b) WB60N > 0.5. The composite-mean map for (a) is displayed in Fig. 6b and that for (b) is in Fig. 6e.

days after WB60N reaches six different threshold values: WB60N < −1, WB60N < −0.5, −0.5 < WB60N < 0, 0 < WB60N < 0.5, WB60N > 0.5, and WB60N > 1 (Fig. 9). It is seen that the composite means of time series of EOF1–EOF6 are close to zero in the period of 1–10 days after a normal meridional mass circulation (i.e., WB60N is between −0.5 and 0.5), consistent with the composite-mean maps shown in Figs. 6a and 6d. The EOF1 and EOF4 modes, as well as the EOF3 and EOF6

modes to a certain degree, represent oscillations between the positive phase when WB60N > 0.5 and the negative phase when WB60N < −0.5. This indicates that the polarity of these four EOF modes highly depends on day-to-day intensity variations of the meridional mass circulation crossing 60°N.

The relative contribution from each EOF mode to the composite-mean maps of SATA at different threshold values of the WB60N index can be obtained from the product of the composite mean of its time series (Fig. 9) and the map correlation of its spatial pattern (Fig. 8) with one of the composite-mean maps (Fig. 6). Note that by design, the sum of contributions to each of the composite-mean maps from individual EOFs over all EOF modes equals 100%. As indicated in Fig. 10, other than for the cases when the meridional mass circulation is normal (i.e., WB60N is between −0.5 and 0.5) in which the amplitude of the composite-mean SATA is close to zero, the EOF1 and EOF4 modes have the largest contributions (more than 70%) to the composite-mean maps of SATA in both the cold air charge and discharge periods. These two modes describe the synoptic scenario that more polar cold air migrates away from the Arctic into the two major continents during the cold air discharge period (i.e., 1–10 days after WB60N > 0.5) and vice versa. The amplitude variation of these two EOF modes gives rise to the case-to-case amplitude variation of SATA about the composite-mean spatial pattern, explaining part of the case-to-case differences.

The other modes, although contributing little to the composite-mean pattern, may still contribute to the case-to-case variation of SATA about the composite means associated with different intensity of mass circulation crossing 60°N. The spatial pattern of EOF2 indicates that North America experiences abnormal cold but most of Eurasia has warm SATA for the positive phase of EOF2 and the reverse is true for the negative phase. According to Fig. 9, the composite means of the EOF2 time series are close to zero for all threshold values of WB60N, suggesting little phase preference of EOF2 to different intensity of meridional mass circulation across 60°N. The positive phase of EOF3 is characterized with an anomalous warm center over the Arctic that is oriented toward Eurasia with abnormal cold only over the midlatitude of Eurasia but over the entirety of North America. The opposite pattern is found for the negative phase of EOF3. The EOF5 mode exhibits a wavenumber-2 pattern with opposite signs between the western and eastern halves of the continents north of 45°N, where the spatial pattern of EOF6 is dominated by wavenumber 3. To some extent, these two modes represent temperature anomalies resulting from the presence of large-amplitude quasi-stationary waves
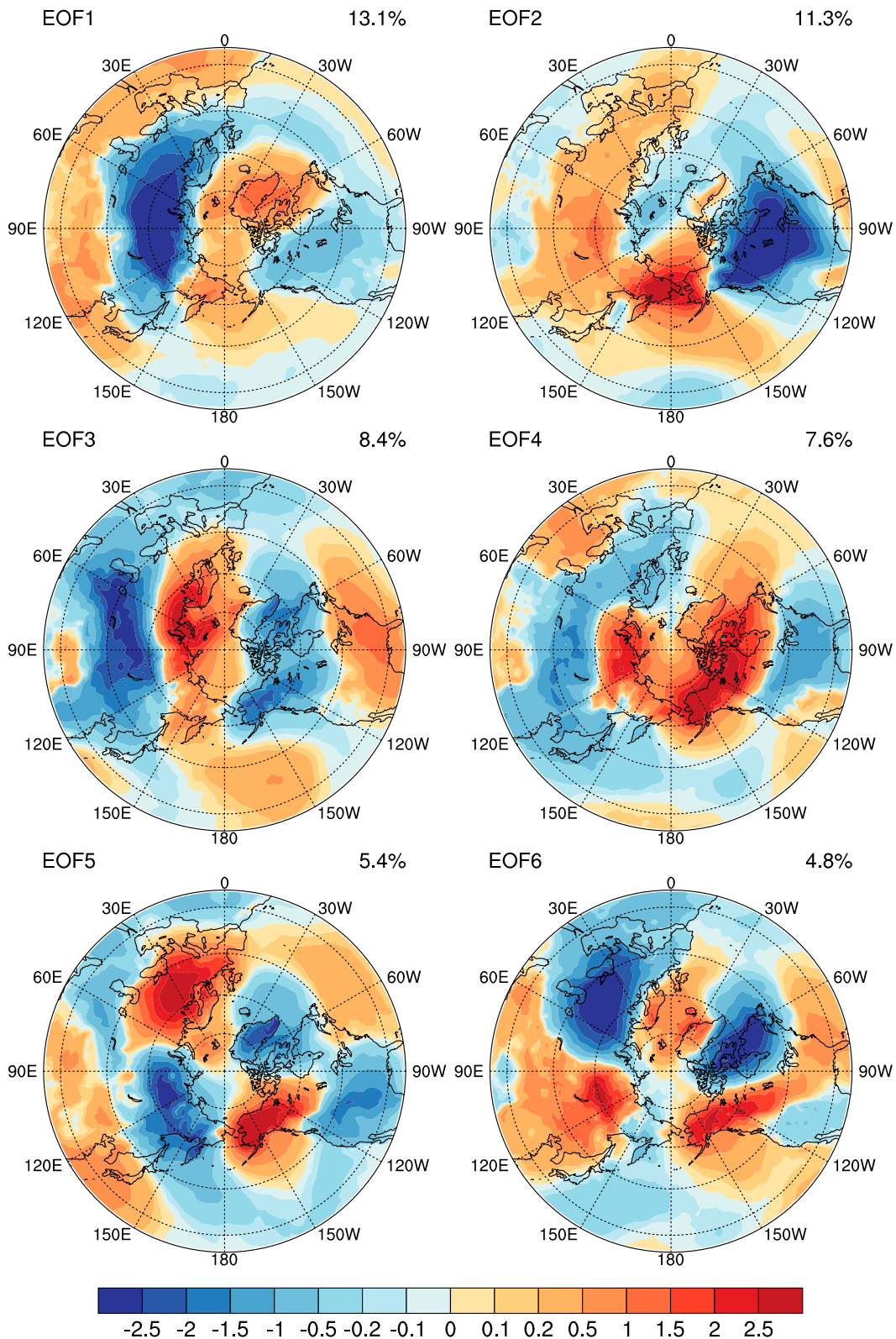
FIG. 8. Spatial patterns of the first six EOF modes of SATA over the domain 25°–90°N for the 32 winters during 1979–2011.
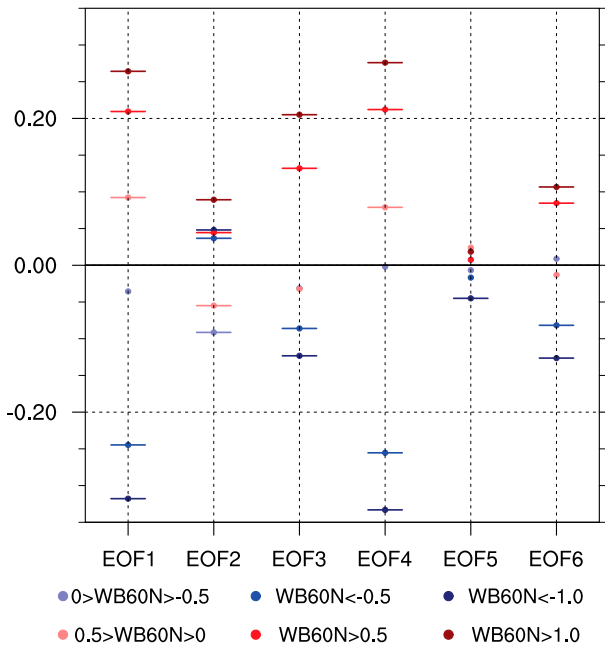
FIG. 9. Composite means (K, ordinate) of the time series of the first six EOF modes for all cases in the period of 1–10 days after the WB60N index, reaching these six threshold values specified in the color-coded figure legend. The results with short horizontal bars exceed the 95% confidence intervals.

during the cold air discharge period and weak quasi-stationary waves during the cold air charge period.

To examine if those EOF modes that contribute little to the composite-mean pattern (e.g., EOF2) may still have a robust and physical association with the WB60N index, we calculate the contribution to the total variance of each EOF mode from different amplitude for three situations: (i) all days in the 32 winters (climatology, dashed black curves in Fig. 11), (ii) in the cold air charge period or 1–10 days after weaker circulation (WB60N < −0.5, blue curves), and (iii) in the cold air discharge period or 1–10 days after strong circulation (WB60N > 0.5, red curves). We note that for a PDF in which the maximum probability is centered in the middle, such as a normal distribution, its variance distribution has two peaks, one in the middle of the negative range and the other in the middle of the positive range with equal magnitude. In other words, events with moderate-to-large amplitude contribute more to the total variance of the time series even though they occur less frequently than small-amplitude events. Events with extremely large amplitude also contribute little to the total variance owing to their rare occurrence. According to Figs. 11a and 11d, the contribution to the total variance of the EOF1 and EOF4 modes shifts significantly compared to the normal condition: more from large-amplitude negative events (about −1.25 SD) than

large-amplitude positive events (about 1.25 SD) in the cold air charge period, but more so from large-amplitude positive events in the cold air discharge period. Such a shift in the variance distribution diagram from large-amplitude negative events during the cold air charge period to positive events during the cold air discharge period is also accompanied with a shift in the PDFs of the time series of EOF1 and EOF4 toward positive values from negative values as the WB60N index intensifies (not shown). This is another way to describe the oscillation of the EOF1 and EOF4 between the negative phase in the cold air charge period and the positive phase in the cold air discharge period. Such a shift toward large-amplitude positive events in the variance distribution is also found in the EOF3 and EOF6 (Figs. 11c,f), though the two modes explain only a small portion of the total variance of SATA.

The EOF2 mode, characterized by an anticorrelation of SATA between North America and Eurasia, exhibits a distinct relationship with the WB60N index. It has little shift in both probability distribution (not shown but indicated by the very small composite means of its time series as shown in Fig. 9) and variance distribution (Fig. 11b) toward positive or negative events. However, there is a noticeable increase in the variance explained by the EOF2 mode from 9% in the cold air charge period for WB60N < −0.5%–13% in the cold air discharge period for WB60N > 0.5. Most of the increase of the EOF2-explained variance in the cold air discharge period comes from large-amplitude (about 1.5 SD) events of both signs. This suggests that another prominent spatial pattern of SATA in response to a stronger mass circulation crossing 60°N is the occurrence of massive cold air outbreaks over one of the two continents but pronounced warmth in the other continent. For a weaker meridional circulation crossing 60°N, the anticorrelated spatial pattern of SATA between the two continents may still take place but with a much weaker amplitude.

6. Concluding remarks

We have investigated the daily variability of anomalous warmth and cold over the domain 25°–90°N in winter seasons and its relation to the meridional mass circulation variability using the ERA-Interim data from November to February in 1979–2011. We have constructed two mass circulation indices: one (denoted as WB60N) for measuring day-to-day variations of the total poleward mass transport crossing 60°N into the Arctic upper troposphere and stratosphere by the warm air branch and the other (CB60N) for the total equatorward mass transport crossing 60°N out of the Arctic
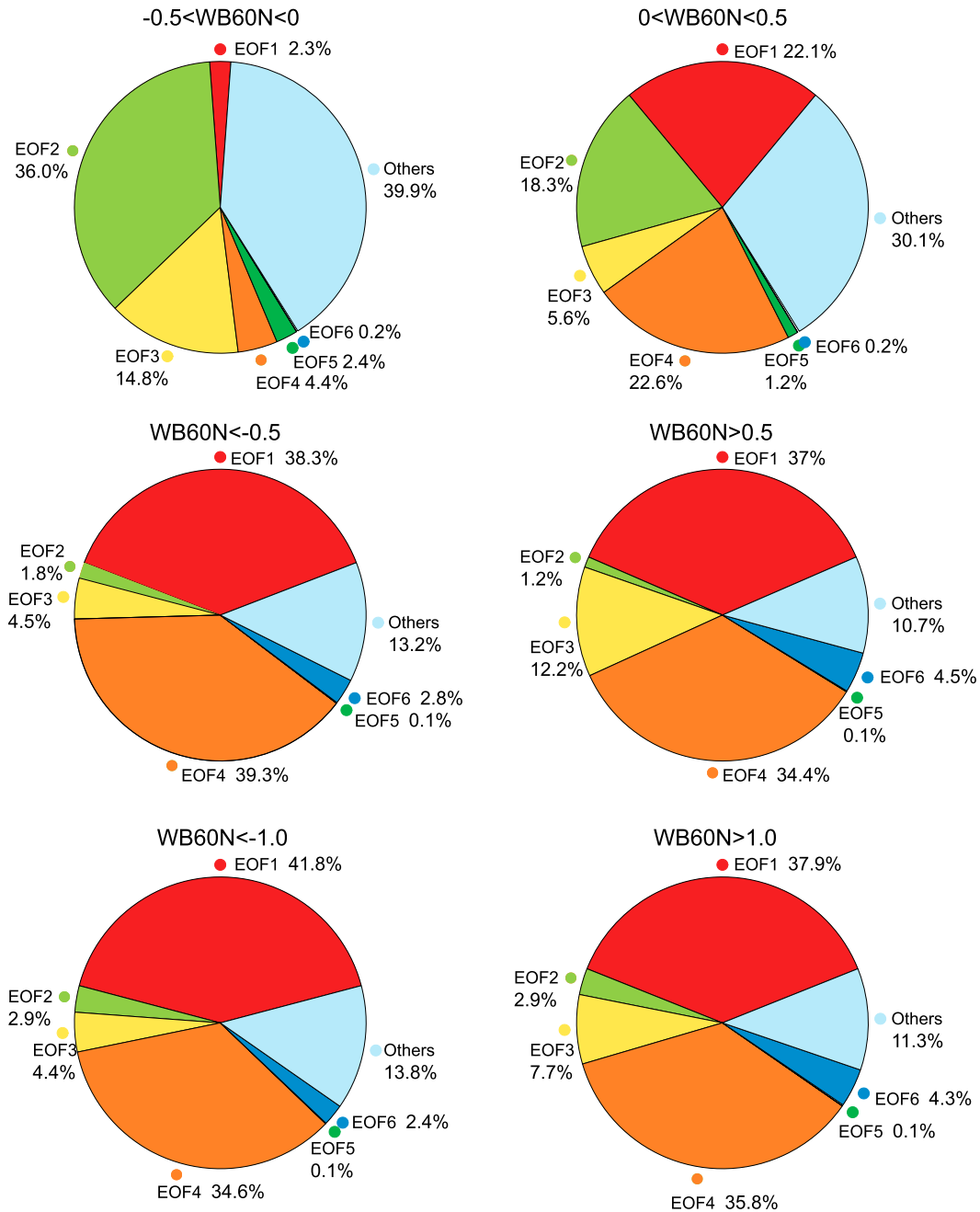
FIG. 10. The relative contributions from each EOF mode to the composite-mean maps shown in Fig. 6 (see text for details).

by the cold air branch in the lower troposphere. These two indices not only have a nearly perfect positive correlation with one another with little lead/lag on average, but also have the same amplitude of day-to-day variations. This indicates that a stronger poleward warm airmass circulation into the polar region tends to be compensated by a stronger equatorward mass transport by the cold air branch below and vice versa. Such synchronization of day-to-day variations of CB60N with WB60N is expected from the meridional mass circulation theory (e.g., Johnson 1989), namely, that stronger westward-tilting wave activities in the extratropics result in a simultaneous increase both in poleward mass transport into the polar region aloft and in equatorward mass transport out of the polar region in the lower troposphere and vice versa.
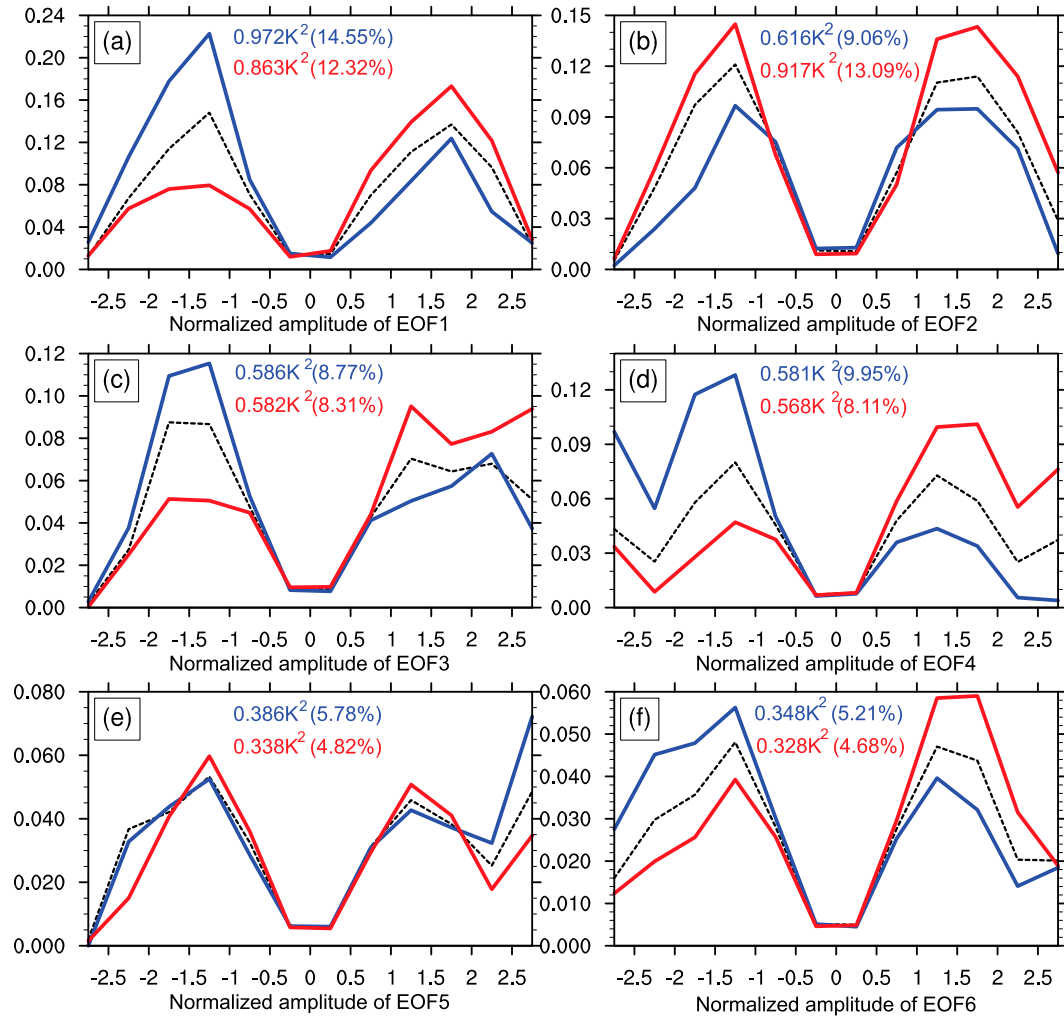
FIG. 11. Variance distribution diagrams showing the contribution to the total variance (K^2, ordinate) of an EOF mode of SATA from the different amplitudes of its normalized time series for (a) EOF1, (b) EOF2, (c) EOF3, (d) EOF4, (e) EOF5, and (f) EOF6. Dashed black curves are obtained for all days in the 32 winters (climatological condition). Blue curves are obtained for all cases in the period of 1–10 days after WB60N < −0.5, whereas red curves are for all cases after WB60N > 0.5. The variance and the percentage of variance explained by each EOF mode for all cases in the period of 1–10 days after WB60N < −0.5 is indicated by numbers in blue, and those for cases after WB60N > 0.5 is indicated by numbers in red.

We have also developed four temperature area indices to measure the continental-scale anomalous warmth and cold at the surface in high latitudes and midlatitudes. Specifically, we have constructed indices W_H and C_H on a daily basis, where W_H corresponds to the percentage of the area in high latitudes (60°–90°N) occupied by SATA > 0.5 LSD (warm surface air temperature anomalies that exceed 0.5 local standard deviation) and C_H is the percentage of the area in high latitudes occupied by SATA < −0.5 LSD (cold surface air temperature anomalies that are less than −0.5 local standard deviation). Similarly, we have constructed indices W_M and C_M to measure the percentage of the area

in midlatitudes (25°–60°N) occupied by SATA > 0.5 LSD and SATA < −0.5 LSD, respectively. The WB60N index is highly positively correlated with the W_H and C_M indices when the WB60N index leads by 1–10 days. Meanwhile, with the same lead time, the WB60N index is highly negatively correlated with the C_H and W_M indices. There exists a systematic shift in the probability distribution function of each of the four temperature area indices. Under a normal condition in which the amplitude of WB60N is near zero, all of the four temperature area indices exhibit a quasi-normal probability distribution that is centered at the climatological value (about 30.85%). In the period of 1–10 days after WB60N

is above the normal by 0.5 standard deviations, the center of the quasi-normal probability distribution functions of both C_M and W_H indices shift toward a value larger than 30.85%, while the center of the quasi-normal probability distribution functions of both C_H and W_M shifts toward a smaller value. The magnitude of such a shift increases as the amplitude of the WB60N increases. Such shifts in PDF are found toward the other direction in the period of 1–10 days after WB60N is below the normal by 0.5 standard deviations or more. These results indicate that the cold air is largely imprisoned within the Arctic region during the cold air charge period, responsible for the prevalence of warmth in midlatitudes and cold in high latitudes. Conversely, during the cold air discharge period, a stronger warm air transport into the polar upper atmosphere is accompanied by a stronger equatorward advancement of cold air near the surface, resulting in massive cold air outbreaks in midlatitudes and anomalous warmth in high latitudes. For this reason and following Namias (1950), we refer to the period of 1–10 days after a stronger meridional mass circulation crossing 60°N as the cold air discharge period and that after a weaker meridional circulation as the cold air charge period.

The robust correlations between the circulation and temperature area indices can be further substantiated from the dominant geographical patterns of SATA that are negatively correlated between the cold air charge and discharge periods. During the cold air discharge period, the probability of occurrence for warm SATA increases substantially over the entire Arctic region at the expense of pronounced decrease in cold SATA. In the midlatitudes, in contrast, there is a pronounced increase in the probability of occurrence for cold SATA and a decrease in the probability of warm SATA. The opposite spatial pattern of the probability of occurrence for warm and cold SATA is found for the cold air charge period. Such a reversal of the spatial pattern of SATA from the cold air charge to discharge period is also found in the composite-mean maps of SATA. The amplitude of the opposite composite patterns increases with the increase of the amplitude of the WB60N index, indicating more extreme cold SATA over the midlatitudes in the cold air charge period after a stronger mass circulation crossing 60°N and vice versa.

The spatial pattern of large-amplitude cold SATA over both continents during the cold air discharge period can be linked to more occurrences of large-amplitude positive events of the EOF1 and EOF4 modes of daily SATA over the domain 25°–90°N in winter seasons. Beside this dominant pattern of SATA, there is another dominant but distinct spatial pattern of SATA during the cold air discharge period, namely, that massive cold air outbreaks mainly take place over one of the two continents with abnormal warmth over the other continent, corresponding to the EOF2 mode of SATA in winter seasons. The EOF2 mode contributes to large-amplitude SATA during the cold air discharge period with larger amplitude of both positive and negative events than during the cold air charge period in which the variance associated with the EOF2 mode is reduced greatly.

The results presented in this paper demonstrate that the day-to-day variability of meridional mass circulation crossing subpolar latitudes can be used as a precursor index for cold air outbreak events. It is directly related to cold air outbreaks in midlatitudes both in terms of mean values and their probability distribution. In addition, the day-to-day variability of mass circulation crossing subpolar latitudes seems to explain the origin of the dominant EOF modes of daily surface air temperature anomalies in winter. The day-to-day variability of poleward mass circulation in the warm air branch can be further related to tropical forcing and stratospheric circulation anomalies as elicited in the studies on global mass circulation (e.g., Johnson 1989; Schneider 2006; Pauluis et al. 2008; Cai and Shin 2014; and reference therein). In particular, the stratospheric mass circulation variability is linked to the tropical circulation anomalies via the poleward propagation signal (Cai and Ren 2007). One of the future research areas is to investigate the associations of cold air outbreaks with anomalies in upper-tropospheric mass circulation, stratospheric mass circulation, and tropical circulation anomalies. As the mass circulation indices measure the net mass exchange between high and midlatitudes in each of the warm and cold air branches, they should have a close relation with other well-established circulation indices describing the north–south pressure gradient or the extratropical westerly jet in the Northern Hemisphere, such as the zonal, AO/NAO, and NAM indices. Those circulation indices are strongly associated with winter cold air outbreaks as demonstrated in the references cited in the introduction. It is our belief that the mass circulation indices can bring richer, more direct, and more statistically robust information on cold air outbreaks in midlatitudes in winter seasons because the connection between the meridional mass circulation and cold air outbreaks is more physical and obvious than the other indices such as the AO or NAM indices. We will carry out a comprehensive study on the relation of mass circulation indices with other circulation indices to confirm this conjecture.

REFERENCES

Andrews, D. G., and M. E. McIntyre, 1976: Planetary waves in horizontal and vertical shear: The generalized Eliassen-Palm relation and the mean zonal acceleration. *J. Atmos. Sci.,* **33,** 2031–2048, doi:10.1175/1520-0469(1976)033<2031:PWIHAV>2.0.CO;2.

Baldwin, M. P., and T. J. Dunkerton, 1999: Propagation of the Arctic Oscillation from the stratosphere to the troposphere. *J. Geophys. Res.,* **104,** 30 937–30 946, doi:10.1029/1999JD900445.

Boyle, J. S., and T.-J. Chen, 1987: Synoptic aspects of the wintertime East Asian monsoon. *Monsoon Meteorology,* C.-P. Chang and T. N. Krishnamurti, Eds., Oxford University Press, 125–160.

Brugge, R., 1991: The cold snap of February 1991. *Weather,* **46,** 222–231, doi:10.1002/j.1477-8696.1991.tb05752.x.

Cai, M., 2003: Potential vorticity intrusion index and climate variability of surface temperature. *Geophys. Res. Lett.,* **30,** 1119, doi:10.1029/2002GL015926.

——, and R.-C. Ren, 2007: Meridional and downward propagation of atmospheric circulation anomalies. Part I: Northern Hemisphere cold season variability. *J. Atmos. Sci.,* **64,** 1880–1901, doi:10.1175/JAS3922.1.

——, and C.-S. Shin, 2014: A total flow perspective of atmospheric mass and angular momentum circulations: Boreal winter mean state. *J. Atmos. Sci.,* **71,** 2244–2263, doi:10.1175/JAS-D-13-0175.1.

Cellitti, M. P., J. E. Walsh, R. M. Rauber, and D. H. Portis, 2006: Extreme cold air outbreaks over the United States, the polar vortex, and the large-scale circulation. *J. Geophys. Res.,* **111,** D02114, doi:10.1029/2005JD006273.

Chan, J. C., and C. Li, 2004: The East Asia winter monsoon. *East Asian Monsoon,* C.-P. Chang, Eds., World Scientific, 54–106.

Cohen, J., J. Foster, M. Barlow, K. Saito, and J. Jones, 2010: Winter 2009–2010: A case study of an extreme Arctic Oscillation event. *Geophys. Res. Lett.,* **37,** L17707, doi:10.1029/2010GL044256.

Colucci, S. J., and J. C. Davenport, 1987: Rapid surface anticyclogenesis: Synoptic climatology and attendant large-scale circulation changes. *Mon. Wea. Rev.,* **115,** 822–836, doi:10.1175/1520-0493(1987)115<0822:RSASCA>2.0.CO;2.

Dee, D. P., and Coauthors, 2011: The ERA-Interim reanalysis: Configuration and performance of the data assimilation system. *Quart. J. Roy. Meteor. Soc.,* **137,** 553–597, doi:10.1002/qj.828.

Ding, Y., 1990: Build-up, air mass transformation and propagation of Siberian high and its relations to cold surge in East Asia. *Meteor. Atmos. Phys.,* **44,** 281–292, doi:10.1007/BF01026822.

Downton, M. W., and K. A. Miller, 1993: The freeze risk to Florida citrus. Part II: Temperature variability and circulation patterns.

J. Climate, **6,** 364–372, doi:10.1175/1520-0442(1993)006<0364:TFRTFC>2.0.CO;2.

Gallimore, R. G., and D. R. Johnson, 1981: The forcing of the meridional circulation of the isentropic zonally averaged circumpolar vortex. *J. Atmos. Sci.,* **38,** 583–599, doi:10.1175/1520-0469(1981)038<0583:TFOTMC>2.0.CO;2.

Gong, D.-Y., and C.-H. Ho, 2004: Intra-seasonal variability of wintertime temperature over East Asia. *Int. J. Climatol.,* **24,** 131–144, doi:10.1002/joc.1006.

Hayasaki, M., S. Sugata, and H. L. Tanaka, 2006: Interannual variation of cold frontal activity in spring in Mongolia. *J. Meteor. Soc. Japan,* **84,** 463–475, doi:10.2151/jmsj.84.463.

Iwasaki, T., and Y. Mochizuki, 2012: Mass-weighted isentropic zonal mean equatorward flow in the Northern Hemispheric winter. *SOLA,* **8,** 115–118, doi:10.2151/sola.2012-029.

——, T. Shoji, Y. Kanno, M. Sawada, M. Ujiie, and K. Takaya, 2014: Isentropic analysis of polar cold airmass streams in the Northern Hemispheric winter. *J. Atmos. Sci.,* **71,** 2230–2243, doi:10.1175/JAS-D-13-058.1.

Jeong, J.-H., C.-H. Ho, B.-M. Kim, and W.-T. Kwon, 2005: Influence of the Madden-Julian oscillation on wintertime surface air temperature and cold surges in East Asia. *J. Geophys. Res.,* **110,** D11104, doi:10.1029/2004JD005408.

——, B.-M. Kim, C.-H. Ho, and G.-H. Lim, 2006: Stratospheric origin of cold surge occurrence in East Asia. *Geophys. Res. Lett.,* **33,** L14710, doi:10.1029/2006GL026607.

Johnson, D. R., 1989: The forcing and maintenance of global monsoonal circulations: An isentropic analysis. *Advances in Geophysics,* Vol. 31, Academic Press, 43–316, doi:10.1016/S0065-2687(08)60053-9.

Kenyon, J., and G. C. Hegerl, 2008: Influence of modes of climate variability on global temperature extremes. *J. Climate,* **21,** 3872–3889, doi:10.1175/2008JCLI2125.1.

Kiladis, G., and H. Diaz, 1989: Global climatic anomalies associated with extremes in the Southern Oscillation. *J. Climate,* **2,** 1069–1090, doi:10.1175/1520-0442(1989)002<1069:GCAAWE>2.0.CO;2.

Kolstad, E. W., T. Breiteig, and A. A. Scaife, 2010: The association between stratospheric weak polar vortex events and cold air outbreaks in the Northern Hemisphere. *Quart. J. Roy. Meteor. Soc.,* **136,** 886–893, doi:10.1002/qj.620.

Konrad, C. E., 1996: Relationships between the intensity of cold-air outbreaks and the evolution of synoptic and planetary-scale features over North America. *Mon. Wea. Rev.,* **124,** 1067–1083, doi:10.1175/1520-0493(1996)124<1067:RBTIOC>2.0.CO;2.

Kunkel, K. E., R. A. Pielke Jr., and S. A. Changnon, 1999: Temporal fluctuations in weather and climate extremes that cause economic and human health impacts: A review. *Bull. Amer. Meteor. Soc.,* **80,** 1077–1098, doi:10.1175/1520-0477(1999)080<1077:TFIWAC>2.0.CO;2.

Namias, J., 1950: The index cycle and its role in the general circulation. *J. Meteor.,* **7,** 130–139, doi:10.1175/1520-0469(1950)007<0130:TICAIR>2.0.CO;2.

Park, T.-W., J.-H. Jeong, C.-H. Ho, and S.-J. Kim, 2008: Characteristics of atmospheric circulation associated with cold surge occurrences in East Asia: A case study during 2005/06 winter. *Adv. Atmos. Sci.,* **25,** 791–804, doi:10.1007/s00376-008-0791-0.

Pauluis, O., A. Czaja, and R. Korty, 2008: The global atmospheric circulation on moist isentropes. *Science,* **321,** 1075–1078, doi:10.1126/science.1159649.

——, ——, and ——, 2010: The global atmospheric circulation in moist isentropic coordinates. *J. Climate,* **23,** 3077–3093, doi:10.1175/2009JCLI2789.1.

——, T. Shaw, and F. Lalibertéé, 2011: A statistical generalization of the transformed Eulerian-mean circulation for an arbitrary vertical coordinate system. *J. Atmos. Sci.,* **68,** 1766–1783, doi:10.1175/2011JAS3711.1.

Portis, D. H., M. P. Cellitti, W. L. Chapman, and J. E. Walsh, 2006: Low-frequency variability and evolution of North American cold air outbreaks. *Mon. Wea. Rev.,* **134,** 579–597, doi:10.1175/MWR3083.1.

Ren, R.-C., and M. Cai, 2007: Meridional and vertical out-of-phase relationships of temperature anomalies associated with the northern annular mode variability. *Geophys. Res. Lett.,* **34,** L07704, doi:10.1029/2006GL028729.

——, and ——, 2008: Meridional and downward propagation of atmospheric circulation anomalies. Part II: Southern Hemisphere cold season variability. *J. Atmos. Sci.,* **65,** 2343–2359, doi:10.1175/2007JAS2594.1.

Rogers, J. C., and R. V. Rohli, 1991: Florida citrus freezes and polar anticyclones in the Great Plains. *J. Climate,* **4,** 1103–1113, doi:10.1175/1520-0442(1991)004<1103:FCFAPA>2.0.CO;2.

Rosenzweig, C., A. Iglesias, X.-B. Yang, P. R. Epstein, and E. Chivian, 2001: Climate change and extreme weather events; Implications for food production, plant diseases, and pests. *Global Change Hum. Health,* **2,** 90–104, doi:10.1023/A:1015086831467.

Ryoo, S.-B., W.-T. Kwon, and J.-G. Jhun, 2005: Surface and upper-level features associated with wintertime cold surge outbreaks in South Korea. *Adv. Atmos. Sci.,* **22,** 509–524, doi:10.1007/BF02918484.

Schneider, T., 2006: The general circulation of the atmosphere. *Annu. Rev. Earth Planet. Sci.,* **34,** 655–688, doi:10.1146/annurev.earth.34.031405.125144.

Shabbar, A., and B. Bonsal, 2003: An assessment of changes in winter cold and warm spells over Canada. *Nat. Hazards,* **29,** 173–188, doi:10.1023/A:1023639209987.

Takaya, K., and H. Nakamura, 2005: Mechanisms of intraseasonal amplification of the cold Siberian high. *J. Atmos. Sci.,* **62,** 4423–4440, doi:10.1175/JAS3629.1.

Thompson, D. W. J., and J. M. Wallace, 1998: The Arctic Oscillation signature in the wintertime geopotential height and temperature fields. *Geophys. Res. Lett.,* **25,** 1297–1300, doi:10.1029/98GL00950.

——, and ——, 2001: Regional climate impacts of the Northern Hemisphere annular mode. *Science,* **293,** 85–89, doi:10.1126/science.1058958.

——, M. P. Baldwin, and J. M. Wallace, 2002: Stratospheric connection to Northern Hemisphere wintertime weather: Implications for prediction. *J. Climate,* **15,** 1421–1428, doi:10.1175/1520-0442(2002)015<1421:SCTNHW>2.0.CO;2.

Thompson, R. D., 1987: Cold winters in southern England. *Weather,* **42,** 160–161.

Townsend, R. D., and D. R. Johnson, 1985: A diagnostic study of the isentropic zonally averaged mass circulation during the First GARP Global Experiment. *J. Atmos. Sci.,* **42,** 1565–1579, doi:10.1175/1520-0469(1985)042<1565:ADSOTI>2.0.CO;2.

Trenberth, K. E., 1991: Climate diagnostics from global analysis: Conservation of mass in ECWMF analysis. *J. Climate,* **4,** 707–722, doi:10.1175/1520-0442(1991)004<0707:CDFGAC>2.0.CO;2.

van den Dool, H. M., and S. Saha, 1993: Seasonal redistribution and conservation of atmospheric mass in a general circulation model. *J. Climate,* **6,** 22–30, doi:10.1175/1520-0442(1993)006<0022:SRACOA>2.0.CO;2.

Wallace, J. M., 2000: North Atlantic Oscillation/annular mode: Two paradigms—One phenomenon. *Quart. J. Roy. Meteor. Soc.,* **126,** 791–805, doi:10.1002/qj.49712656402.

Walsh, J. E., A. S. Phillips, D. H. Portis, and W. L. Chapman, 2001: Extreme cold outbreaks in the United States and Europe, 1948–99. *J. Climate,* **14,** 2642–2658, doi:10.1175/1520-0442(2001)014<2642:ECOITU>2.0.CO;2.

Wettstein, J. J., and L. O. Mearns, 2002: The influence of the North Atlantic–Arctic Oscillation on mean, variance, and extremes of temperature in the northeastern United States and Canada. *J. Climate,* **15,** 3586–3600, doi:10.1175/1520-0442(2002)015<3586:TIOTNA>2.0.CO;2.

Wexler, H., 1951: Anticyclones. *Compendium of Meteorology,* T. F. Malone, Eds., Amer. Meteor. Soc., 621–628.

Wu, M.-C., and J. C.-L. Chan, 1995: Surface features of winter monsoon surges over south China. *Mon. Wea. Rev.,* **123,** 662–680, doi:10.1175/1520-0493(1995)123<0662:SFOWMS>2.0.CO;2.

Zhang, Y., K. R. Sperber, and J. S. Boyle, 1997: Climatology and interannual variation of the East Asian winter monsoon: Results from the 1979–95 NCEP/NCAR reanalysis. *Mon. Wea. Rev.,* **125,** 2605–2619, doi:10.1175/1520-0493(1997)125<2605:CAIVOT>2.0.CO;2.